7

Joint Inversion of High-Rate GPS and Teleseismic Observations for Rupture Process of the 23 June 2014 (M_w 7.9) Rat Islands Archipelago, Alaska, Intermediate Depth Earthquake

Lingling Ye,[1,2] Thorne Lay,[1] Hiroo Kanamori,[2] Jeffrey T. Freymueller,[3] and Luis Rivera[4]

ABSTRACT

On 23 June 2014, a large (M_w 7.9) earthquake ruptured within the subducting Pacific plate ~100 km below the Rat Islands archipelago, Alaska. The focal mechanism indicates two possible rupture orientations: (1) on a shallowly dipping fault plane (strike 206°, dip 24°, rake -14°) striking perpendicular to the trench, possibly related to curvature of the underthrust slab or (2) on a steeply dipping fault plane (strike 309°, dip 84°, rake -113°) striking parallel to the trench, possibly associated with a slab detachment process. Joint inversion of teleseismic body waves and regional high-rate (1 Hz) GPS recordings indicate a slip zone spanning 50 km × 30 km with a maximum slip of ~11 m on the shallowly dipping plane, or a more distributed slip pattern extending upward to ~70 km, with maximum slip of ~14 m on the steeply dipping plane. Estimated stress drops are 16 to 25 MPa. The radiated energy is ~1.8 × 10^16 J, and the inferred low radiation efficiency, ~0.1, is compatible with the assumed low rupture velocity, 1.5 km/s. The finite-fault models and aftershocks do not indicate a preferred fault plane. This type of intermediate-depth intraslab faulting can be very damaging for populated regions above subduction zones such as Japan, Taiwan, Chile, Peru, and Indonesia.

7.1. INTRODUCTION

Most large subduction zone earthquakes involve shallow thrust faulting offshore on the plate boundary megathrust fault, producing both shaking and tsunami hazards for nearby regions. However, large intraplate earthquakes also occur in subduction zones, including normal-faulting events near the outer trench slope [e.g., *Craig et al.*, 2014; *Lay et al.*, 1989], the largest known example being the great (M_S ~8.3+) 1933 Sanriku-oki earthquake [e.g., *Kanamori*, 1971]. The shaking and tsunami hazard of these near-trench events is now broadly recognized [e.g., *Lay et al.*, 2009, 2011], although the frequency of occurrence of normal-faulting events remains difficult to quantify [e.g., *Sleep*, 2012].

Less well recognized are the hazards presented by large intraslab earthquakes at depths of ~70 km to 130 km, located below the coastline and volcanic arc. While not usually tsunamigenic, the relatively high stress drops and high moment-scaled radiated energy commonly observed for intraplate events [e.g., *Ye et al.*, 2012] can result in strong ground shaking from these intraslab events.

Several great intraslab events have occurred in this depth range (e.g., 4 November 1963 Banda Sea (M_w 8.3) ~120 km deep [*Welc and Lay*, 1987]; 22 June 1977 Tonga

[1]*Department of Earth and Planetary Sciences, University of California Santa Cruz, Santa Cruz, California, USA*

[2]*Seismological Laboratory, California Institute of Technology, Pasadena, California, USA*

[3]*Geophysical Institute, University of Alaska, Fairbanks, Alaska, USA*

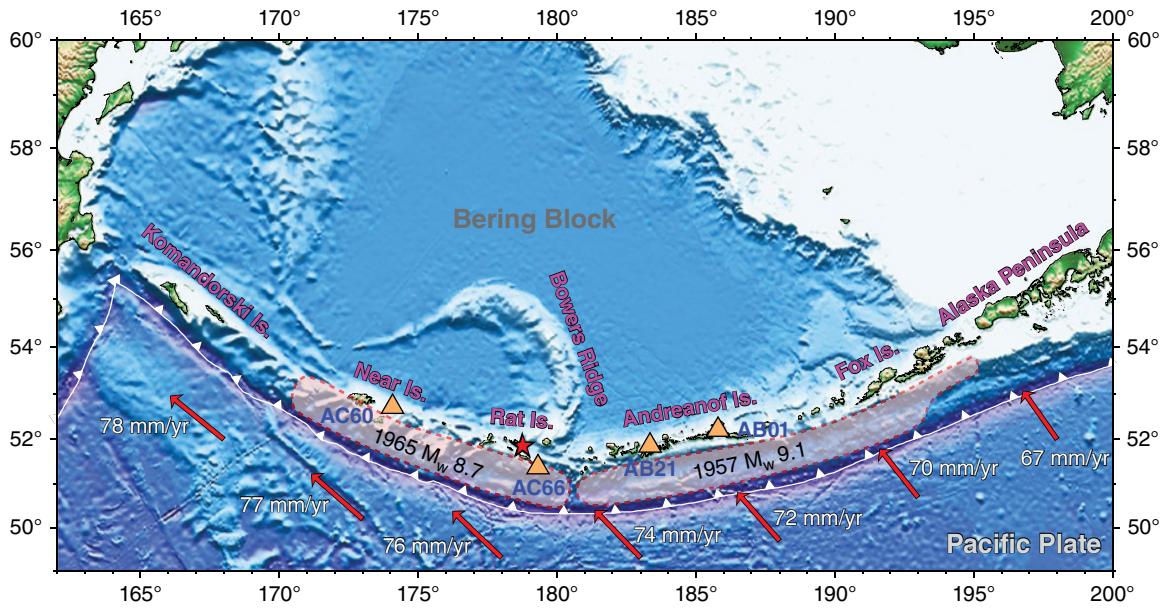[4]*Institut de Physique du Globe de Strasbourg, University of Strasbourg, CNRS, Strasbourg, France*

Figure 7.1 Geographic features of the Aleutian island arc and the Bering block around the 2014 M_w 7.9 Rat Islands earthquake (star) along with the aftershock zones of the 1957 M_w 9.1 and 1965 M_w 8.7 earthquakes [*Sykes*, 1971]. Triangles show the location of the four hr-GPS sites used in the joint inversion. The arrows indicate the motions of the Pacific plate relative to a fixed North America plate (model MORVEL [*DeMets et al.*, 2010]). The Bering block has a westward motion and rotation relative to fixed North America that reduces obliquity of convergence in the Aleutian trench near the Rat Islands.

earthquake (M_w 8.2) ~96 km deep [*Zhang and Lay*, 1989]; M ~8.1 events on 11 August 1903 beneath Kythira, Greece [*Papadopoulos and Vassilopoulou*, 2001] and 15 June 1911 under the Ryukyu Islands [*Allen et al.*, 2009]; 9 December 1950 (M_S 8, M_w 7.9) Antofagasta, Chile, earthquake [*Kausel and Campos*, 1992]; and an M_w 8.3 event on 17 August 1906 near the Rat Islands, Aleutians [*Okal*, 2005]). Recent examples of damaging events of this type include the ~78 km deep 30 September 2009 (M_w 7.6) Indonesia earthquake, which struck near the city of Padang [e.g., *McCloskey et al.*, 2010], taking more than 1100 lives, and the ~95 km deep 13 June 2005 (M_w 7.8) Tarapaca, Chile, earthquake [e.g., *Delouis and Legrand*, 2007].

Comparable size events at these depths have struck beneath Fiji, the Philippines, Hokkaido, Peru, the Solomon Islands, Tonga, and Romania in the past 35 yr. Some large population centers such as Taipei, Taiwan, and Tokyo, Japan, are exposed to risk from this type of intermediate-depth faulting [e.g., *Kanamori et al.*, 2012]. Complex internal slab deformation is usually involved in such events, and the seismic hazard framework of these events is not well defined due to their infrequent occurrence and lack of a straightforward tectonic strain accumulation model.

On 23 June 2014, the largest magnitude (M_w 7.9) intermediate-depth (70 km–300 km) earthquake (51.849°N,

178.735°E, 109 km deep, 20:53:09.7 UTC, USGS/NEIC: http://earthquake.usgs.gov/) to strike the Aleutians in ~109 yr ruptured within the subducting Pacific slab beneath the Rat Islands archipelago of the western Aleutians, Alaska (Fig. 7.1). Due to the large source depth, the earthquake produced only small tsunami amplitudes of ~2 cm ~300 km to the south at DART (Deep-ocean Assessment and Reporting of Tsunamis) site 21414, and run-ups of up to ~10 cm to 20 cm were recorded by tide gauges in Alaska and Hawaii (http://ntwc.arh.noaa.gov).

While fortunately located below an unpopulated region, this event is representative of the intermediate-depth intraslab ruptures that can pose shaking hazards in many subduction zones. Aftershocks spread northwestward from the hypocenter with depths spanning 70–140 km and the USGS/NEIC locations indicate about 50 km horizontal extent of the main aftershock zone (Fig. 7.2b). Two of the largest early aftershocks are isolated shallow strike-slip events to the west (strike-slip focal mechanisms in Fig. 7.2b); apparently these are triggered events in the Aleutian arc crust.

The 2014 earthquake occurred in the underthrust Pacific slab down-dip of the hypocenter of the great 1965 (M_w 8.7) Rat Islands [*Wu and Kanamori*, 1973; *Beck and Christensen*, 1991] and 17 November 2003 (M_w 7.8) interplate events, west of the bend in the central Aleutian arc
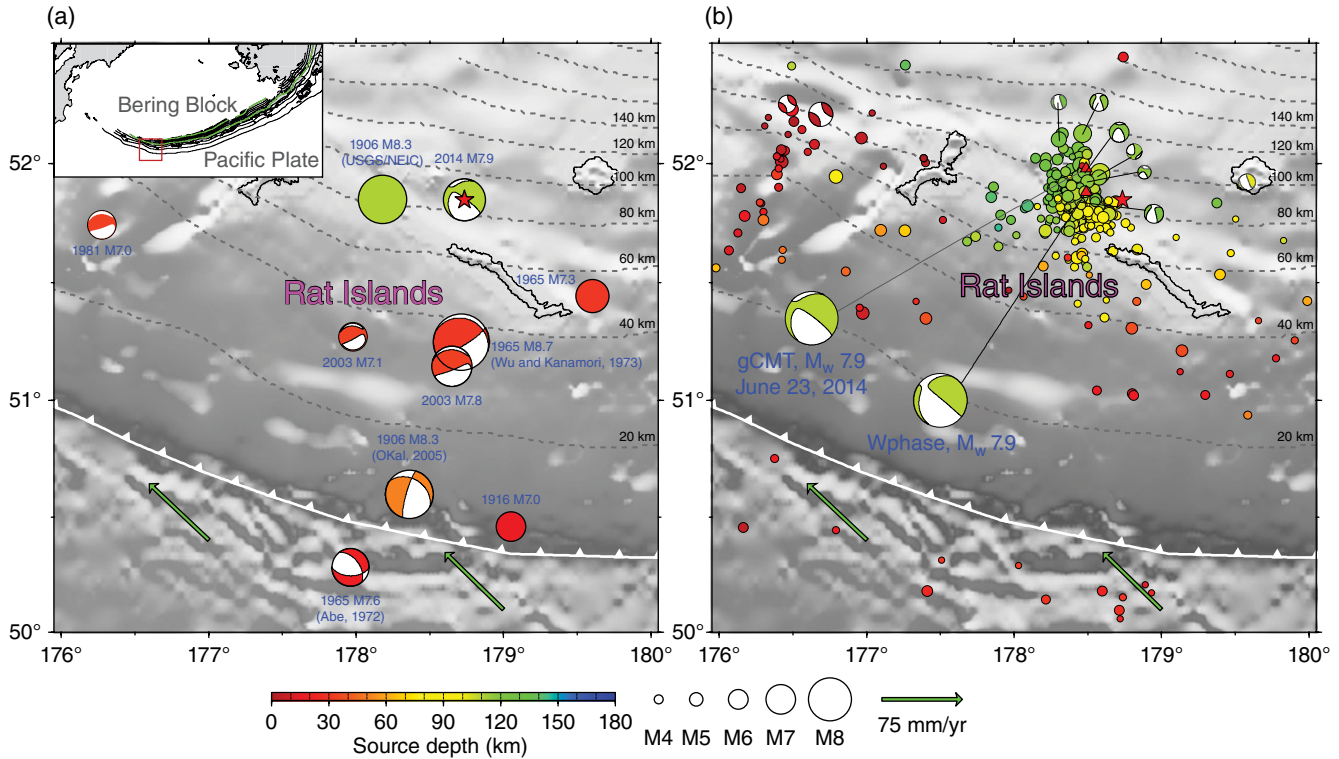
Figure 7.2 (a) Large earthquakes (M ~ 7+) from 1900 to 2014 in the vicinity of the 23 June 2014 M_w 7.9 Rat Islands archipelago earthquake (star). Event locations and magnitudes (circles scaled with magnitude and graytone-coded for depth) are from the USGS/NEIC catalog and focal mechanism solutions from 1976 to 2014 are global Centroid-Moment Tensor (gCMT) solutions. The focal mechanisms for the 1906 *M* 8.3, 1965 *M* 8.7, and 1965 *M* 7.6 events are from *Okal* [2005], *Wu and Kanamori* [1973], and *Abe* [1972], respectively. The inset locates the source region in the western Aleutian Islands, Alaska, with the slab contours indicates the upper surface of the underthrust Pacific slab from model slab 1.0 [*Hayes et al.*, 2012]. (b) Aftershock sequence (circles) of the 2014 M_w 7.9 Rat Islands archipelago earthquake, graytone coded with source depth and scaled proportional to magnitude, including available gCMT solutions. The gCMT and W-phase moment tensor solutions for the main shock are shown along with their associated centroid locations (triangles) relative to the hypocenter from the USGS/NEIC (star). The barbed curve indicates the position of the Aleutian trench. The arrows indicate the highly oblique motion of the Pacific plate relative to a fixed North America plate (model MORVEL [*DeMets et al.*, 2010]).

at around 180°E (Figs. 7.1, 7.2a). This region has right-oblique relative motion between the Pacific and North American plates at ~75mm/yr [e.g., *DeMets et al.*, 2010]. However, rotation or westward extrusion of a "Bering block" relative to North America [e.g., *Mackey et al.*, 1997; *Redfield et al.*, 2007; *Cross and Freymueller*, 2008; *Gabsatarov et al.*, 2011] reduces the rate of the right-oblique component and slightly increases the trench-normal convergence rate along the Rat Islands region [e.g., *Carver and Plafker*, 2008]. *Cross and Freymueller* [2008] favor existence of a separate Bering plate, with arc-parallel translation of 4–8mm/yr and a variable few mm/yr trenchward component of motion in the western Aleutians.

There is evidence for incomplete slip partitioning along the western Aleutians; using the observed rotation of megathrust slip vectors, *Ekström and Engdahl* [1989] estimated that the trench-parallel motion of the arc crust amounted to about 50% of the oblique component of plate motion. This means that the slip vectors for large megathrust earthquakes near the Rat Islands are significantly rotated from both the arc-normal and plate convergence directions (Fig. 7.2a). The arc crust in the western Aleutians is also segmented into blocks with rotations that may locally influence slip partitioning [e.g., *Geist et al.*, 1988; *Ruppert et al.*, 2012] and interplate coupling [*Beck and Christensen*, 1991]. Strike-slip faulting on roughly trench normal faults in the upper plate has

been observed in several locations in the arc, and is likely due to block rotation or other internal deformation of the arc [*Ruppert et al.*, 2012]; the shallow aftershocks located well to the west of the main shock appear to outline one such fault (Fig. 7.2b).

Amchitka Pass (at 180°E) is one of the major block boundaries within the arc [*Geist et al.*, 1988], and it is inferred to be a major structural discontinuity. It separates the slip zones of the 1965 M_w 8.7 and 1957 M_w 9.1 megathrust earthquakes [*Johnson et al.*, 1994] (Fig. 7.1), and *Geist et al.* [1988] identified it as the transition point between arc blocks that were largely rotating in place and arc blocks that were translating westward due to slip partitioning. *Cross and Freymueller* [2008] found an abrupt increase in the degree of slip partitioning observed by GPS measurements on the arc islands at this location, in contrast to the gradual increase of slip partitioning inferred from the slip azimuths for focal mechanisms of megathrust earthquakes. This led them to propose that the roughly arc-parallel strike-slip faults involved in the partitioning were located in the forearc east of Amchitka Pass and crossed into the backarc at Amchitka Pass. The maximum depth of intraslab seismicity also changes from ~250 km east of Amchitka Pass to ~180 km beneath the Rat Islands [*Engdahl et al.*, 1998].

The 17 August 1906 M_w 8.3 earthquake hypocenter is located near the 2014 event in the ISC-GEM catalog [http://www.isc.ac.uk/iscgem/; *Storchak et al.*, 2013], but relocation by *Okal* [2005] shifts it to the south (Fig. 7.2a). The 1906 focal mechanism estimated by *Okal* [2005] has a steeply dipping plane with strike perpendicular to the arc (Fig. 7.2a); plausibly this may have been a slab-tearing event. The data are very limited, so the location, magnitude, and focal mechanism have substantial uncertainty, but *Okal* [2005] suggests that the presence of the Bowers ridge in the upper plate near 180°E (Fig. 7.1) may contribute to strain accumulation and tearing of the subducted slab through collision of the ridge system with the subduction zone.

The 2014 event is the largest intermediate depth event in the Aleutian slab for which extensive geophysical recordings can be used to investigate the source process. This study was motivated by availability of ground motion records from nearby high-rate (1 Hz) GPS (hr-GPS) stations along the arc (Fig. 7.1) and by ambiguity of faulting geometry in an initial teleseismic-only investigation of the source process [*Ye et al.*, 2014]. Few intermediate-depth events have been large enough to be well observed with GPS displacements, and even fewer have had hr-GPS data available. By combining the regional hr-GPS data and teleseismic data, we will improve characterization of the slip distribution for this earthquake, although specification of the fault plane remains uncertain.

7.1.1. Long-Period Point-Source Solutions

Point-source moment tensors for the 2014 Rat Islands earthquake obtained from long-period seismic wave inversions have consistent, predominantly double-couple, source mechanisms with centroid locations about 50 km to the west of the USGS/NEIC hypocenter (Fig. 7.2a). The global Centroid-Moment Tensor (gCMT) solution (http://www.globalcmt.org/CMTsearch.html) has best double-couple nodal planes with strike $\phi_f = 207°$, dip $\delta = 27°$, rake $\lambda = -13°$, and strike $\phi_f = 309°$, dip $\delta = 84°$, rake $\lambda = -117°$, a centroid depth of 104.3 km, a centroid time shift of 24 s, and a seismic moment $M_0 = 9.7 \times 10^{20}$ Nm. We performed a moment tensor inversion of 1 to 5 mHz passband W-phase signals. W-phase inversions provide stable focal mechanisms with little dependence on the earth model [*Kanamori and Rivera*, 2008]. We use 132 ground motion recordings from 58 stations, obtaining a solution with best double-couple nodal planes with $\phi_f = 205.9°$, $\delta = 23.6°$, $\lambda = -14.1°$ and $\phi_f = 308.8°$, $\delta = 84.4°$, and $\lambda = -113.0°$, a centroid depth of 100.5 km, a centroid time shift of 22.9 s, and $M_0 = 1.0 \times 10^{21}$ Nm. These long-period solutions both give M_w 7.9, and both have a null axis striking close to the Pacific-North America relative plate motion direction (Fig. 7.2b), representing either subhorizontal or nearly vertical shearing of the slab.

There is limited resolution of centroid depth for the long-period W-phase inversions (Fig. 7.3a). However, there is greater sensitivity to depth for the fundamental mode Rayleigh waves that arrive after the W-phase window. Fig. 7.3a shows the residual waveform variance of observed minus predicted vertical component Rayleigh wave displacements for a frequency band of 1.667 to 10 mHz for the W-phase inversion solution in the same bandwidth at each target source depth. We compute this for the time window from the end of the W-phase window to the 2.3 km/s group velocity arrival time (latest dots in Fig. 7.3b).

Note the excellent prediction of the Rayleigh waveforms for the 100 km deep source. PREM [*Dziewonski and Anderson*, 1981] is used in these calculations, but for frequencies lower than 10 mHz only small propagation errors due to neglecting aspherical Earth structure are expected for the propagation distances less than 90° used in the inversion. Point-source depths around 100 km to 110 km give the best fits to the long-period Rayleigh waves (Fig. 7.3a), compatible with the long-period inversion centroid estimates.

Non-double-couple components caused by superposition of subevents with different double couples have often been observed for large intermediate-depth and deep earthquakes [e.g., *Kuge and Kawakatsu*, 1992]. The long-period moment tensors for the 2014 Rat
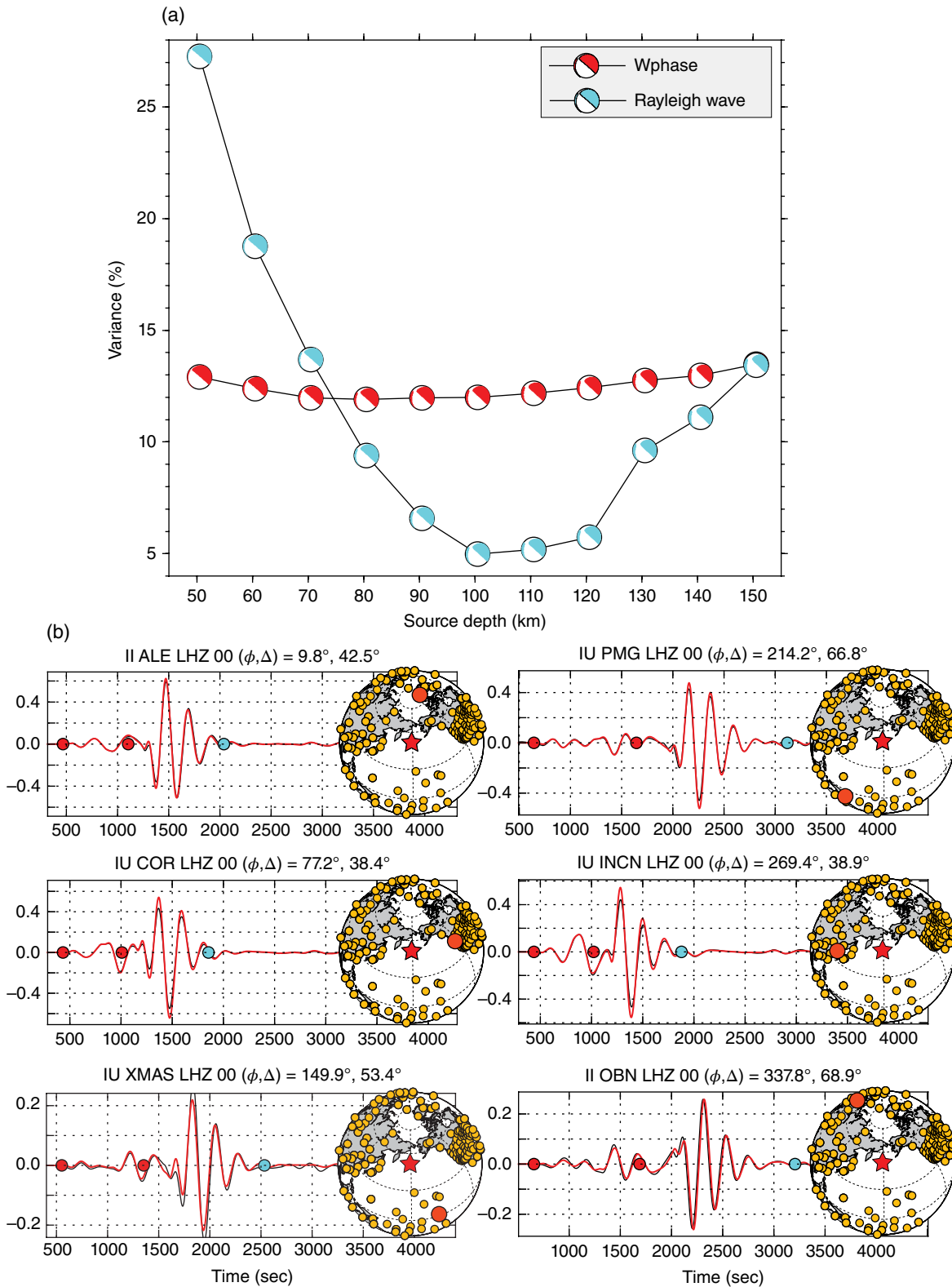
Figure 7.3 (a) Residual waveform variance of W-phase inversions (darker focal mechanisms) using three-component observations in the period range 100–600 s for varying assumed source depths for the 2014 Rat Islands earthquake. The lighter focal mechanisms show the residual waveform variance for predicted vertical component Rayleigh waves in the period range 100–600 s for the W-phase solution at each source depth. (b) Example W-phase (waveform intervals between darker dots) and Rayleigh wave (waveform intervals between second dot and lighter dot) observations (black traces) and computed waveforms (gray traces) for the point-source moment tensor solution at 100.5 km for the 2014 Rat Islands earthquake. The maps indicate the position of each station (big dots) among the total set of stations (smaller dots) used in the corresponding W-phase inversion. Comparable waveform matches are found for all of the stations indicated in the maps.

Islands event do not have significant non-double-couple components, but the body waves do have weak early amplitudes for about 15 s, raising the possibility of some initial mechanism change.

To evaluate this, we applied multiple point-source iterative deconvolution [*Kikuchi and Kanamori*, 1991] to teleseismic body waves filtered in the frequency band of 0.005 to 1 Hz. The largest moment subevents from this inversion have mechanisms similar to the long-period best double-couple solutions and locate ~45 km to the west from the hypocenter, consistent with the centroid locations from the gCMT and W-phase inversions, and with short-period P wave back-projection images [*Ye et al.*, 2014]. The iterative inversions do not fit the first 15 s of low amplitude P wave ground motions very well and variable mechanisms are found for small subevents, but these are not very stable and are influenced by precise alignment of the weak P wave onsets. A W-phase inversion of the first 15 s of long-period ground motions yields a focal mechanism that is close to the overall solution. Overall, it is hard to resolve any change in mechanism during the rupture, or to identify complexity such as en echelon faulting with similar orientations, so we will proceed to model the rupture using single fault planes, acknowledging that there is a possibility of more complex faulting, particularly in the early phase of the rupture.

7.1.2. Finite-Fault Modeling

Guided by the long-period point-source solutions, we determine finite-fault rupture models for the 2014 Rat Islands earthquake by joint inversion of teleseismic body waves and regional hr-GPS (1 Hz) recordings, including long time averaged estimates of their static displacement offsets. We use the least-squares kinematic inversion method with positivity constraint for specified fault geometry, constant rupture expansion velocity (V_r), variable subfault rakes, and subfault source time functions parameterized by several overlapping triangles developed by *Hartzell and Heaton* [1983] and *Kikuchi and Kanamori* [1991].

The teleseismic P and SH waves used in the inversion are the same as those analyzed by *Ye et al.* [2014]. These include ground displacements for 63 P waves and 49 SH waves, filtered in the frequency band 0.005 to 1 Hz.

Regional ground motions were recorded at four GPS stations, AC60, AC66, AB21, and AB01 (Fig. 7.1), along the Aleutian arc. Site AC66 is only ~60 km eastward from the USGS/NEIC epicenter, and provides sensitivity to absolute location of the faulting. Daily positions were estimated in the ITRF2008 reference frame using the GIPSY-OASIS software in point positioning mode [*Zumberge et al.*, 1997], following the analysis methods described in *Fu and Freymueller* [2012].

The three-component coseismic static offsets for all four stations are obtained by the difference of the average daily positions for 5 days before and 5 days after the earthquake, skipping the day of the earthquake (we call these the final static offsets to distinguish them from static offsets estimated from the hr-GPS solutions after passage of the seismic waves).

These offsets may include minor afterslip contribution, but comparison with the hr-GPS estimates indicates that any such contribution is small. AC66 subsided 3.3 ± 0.2 cm and AC60 showed 0.6 ± 0.2 cm subsidence. AB01 also shows subsidence but this may be short-term noise, as a longer time series shows no systematic offset at the time of the event; horizontal displacements at this site are within 1 sigma of zero. Horizontal motions at AC66 are 3.6 ± 0.1 cm to the northwest, and at AC60 are 1.7 ± 0.1 cm to the west. AB21 shows small SE-directed motion but has a very low signal-to-noise ratio.

The hr-GPS solutions with 1 s time sampling were obtained using a kinematic Precise Point Positioning (PPP) approach following the methods described in *Ding et al.* [2015]. We used the GIPSY software with very similar models as in the static processing, except that we used the JPL high rate clock products interpolated from 30 s to 1 s sampling, and estimated the station positions with a random walk noise model. The hr-GPS solutions for this event have slightly higher noise levels than the solutions for the 2013 Craig earthquake [*Ding et al.*, 2015], perhaps because of the remote location relative to sites used in JPL's global orbit and clock solution. Estimates of the static offsets from the hr-GPS kinematic solutions have a noise level of about ± 1 cm due to oscillatory variations seen in the solutions after the passage of the seismic waves. By comparing the final static offset estimates and the offsets several minutes after the origin in the hr-GPS solutions, along with assessing the signal to noise character of each component, we assign different weights to the GPS data for the joint inversions. Among the GPS observations, both hr-GPS signals and static offsets of the NS and EW components at sites AC60 and AC66 (which have amplitudes of several cm), and the vertical static offset at site AC66 are given full weight. The EW components (hr-GPS and static offset) at more distant sites AB01 and AB21 are given a lower weight (about one-third), in the joint inversions. The other components, which have too little signal, are not used in the joint inversion, although we show comparisons of all observed data with the inverted model predictions. The estimated models do predict near-zero static displacements for these remote sites, even though the data were not included in the inversion.

The Green's functions for both teleseismic and GPS modeling are computed for a structural model with a simple 34.5 km thick crust with 0.5 km thick low-velocity

sedimentary layer from Crust 2.0 model [*Bassin et al.*, 2000] underlain by PREM mantle structure. Complete ground motion Green's functions including time-varying and static offsets for the regional hr-GPS signals are computed using a frequency–wave number (F-K) integration method [Computer Programs in Seismology, Robert Herrmann; *Hermann*, 2013]. We low-pass filter the observed hr-GPS signals and the Green's functions with a single-pass Butterworth filter with a corner of 0.05 Hz to eliminate wave energy that cannot be well modeled with a 1D structure. Given that the crustal structure is uncertain, we also perform inversions using the PREM structure for both crust and mantle, finding negligible differences in modeling the hr-GPS and static offsets from the local crustal structure used.

The data lack strong directivity effects, making it difficult to resolve the rupture velocity. Based on our earlier investigation with back-projection imaging and body wave inversion [*Ye et al.*, 2014], we adopt a rupture expansion velocity of 1.5 km/s. The subfault source time functions are parameterized by three overlapping triangles with 3 s rise time and 3 s time shifts, giving 12 s possible subfault source durations. The rupture expansion velocity defines the initiation time of the first triangle for each subfault, which need not be activated in the inversion, allowing for a variable actual rupture velocity. We modify the teleseismic body wave inversion code to include the weighted hr-GPS signals and static displacement offsets, and add a constraint to minimize the difference of the inverted total seismic moment from the long-period seismic moment estimate ($\sim 1.0 \times 10^{21}$ Nm). The effect of the seismic moment constraint is small for this event.

The teleseismic data, regional hr-GPS signals, and static offsets are relatively weighted by balancing signal power contributions of the observations and the coefficient matrix used to assign the relative weight of each data set. We empirically explore modifications of the relative weighting, but given the limited number of GPS observations and the good fits obtained across the suite of data, the precise relative weighting of data sets is not too important in this case. Given that there is no strong constraint to favor either possible fault plane from the seismological data or aftershock locations [*Ye et al.*, 2014], finite-fault inversions for both nodal planes from our W-phase inversion are performed.

The regional hr-GPS ground motions at site AC66 provide valuable constraints on the absolute placement of the fault geometry due to the proximity of the station. This is particularly the case for the steeply dipping fault plane choice, as there is limited horizontal fault width extent and small variation of up-going radiation pattern to AC66. Fig. 7.4 shows waveform predictions for the NS and EW components at AC66 for joint inversions of all data using steeply dipping fault planes with hypocentral locations shifted along SW-NE offsets from the USGS/NEIC hypocenter. Models with the initial rupture location at the USGS/NEIC hypocenter (Model B) or shifted northeastward (Model A), can not match the early motion on the NS component, or the entire EW motion at AC66, and there are strong mismatches of the final static offsets as well. This could be interpreted as favoring the shallowly dipping fault plane choice, as the AC66 fits are much better for that option for corresponding hypocenters, but the absolute location of the USGS/NEIC hypocenter is subject to bias due to slab structure, which should tend to pull the hypocenter estimate in the downdip (northeastward) direction. We explore modest hypocentral shifts to the southwest to evaluate whether the signals at AC66 can be reconciled with the steeply dipping fault plane choice. There is progressive improvement in the prediction of both hr-GPS recordings and static offsets at AC66 as the hypocenter (and rupture plane) shifts to the southwest, and very good agreement is obtained for shifts larger than ~20 km (Models D and E).

To systematically explore the spatial sensitivity to the precise fault positioning for different data sets, we perform finite-fault joint inversions for different assumed hypocentral locations over a 0.05°-spaced grid of longitude and latitude positions around the USGS/NEIC epicenter for both choices of fault plane. Fig. 7.5a and b show that the teleseismic body waves can be well fit in joint inversions with either shallowly or steeply dipping fault plane with almost no resolution of the placement of the fault. The shallowly dipping fault inversions can fit both hr-GPS signals and static offsets very well with epicenters close to the USGS/NEIC location or slightly to the west (Fig. 7.5a), so the total waveform misfit does not favor a specific hypocentral location for the shallowly dipping plane. On the other hand, there is an abrupt spatial change in the residual misfit for the hr-GPS and static offsets for the steeply dipping fault solutions (dominated by the fit to station AC66), as expected given the results in Fig. 7.4. Shifts of the hypocenter of more than 15 km are required for the fit to the GPS data to be acceptable.

Some regional short-period P arrivals at stations along the east-west trending island arc were used in the USGS/NEIC hypocenter location, so the error in the hypocenter is expected to be fairly small, but hypocentral depth and position can still trade off and are subject to errors from the velocity model and nonuniform coverage.

For our final models, we adopt a hypocenter ~25 km SW of the USGS/NEIC solution for both fault planes, as this gives good matches for all data sets. Given that the steep plane can fit the data well only if the hypocenter is shifted from the USGS/NEIC location, a more accurate relocation using a 3-D velocity model might be able to rule out the steep plane if it can rule out this location. There is slightly better fit for the shallowly dipping fault
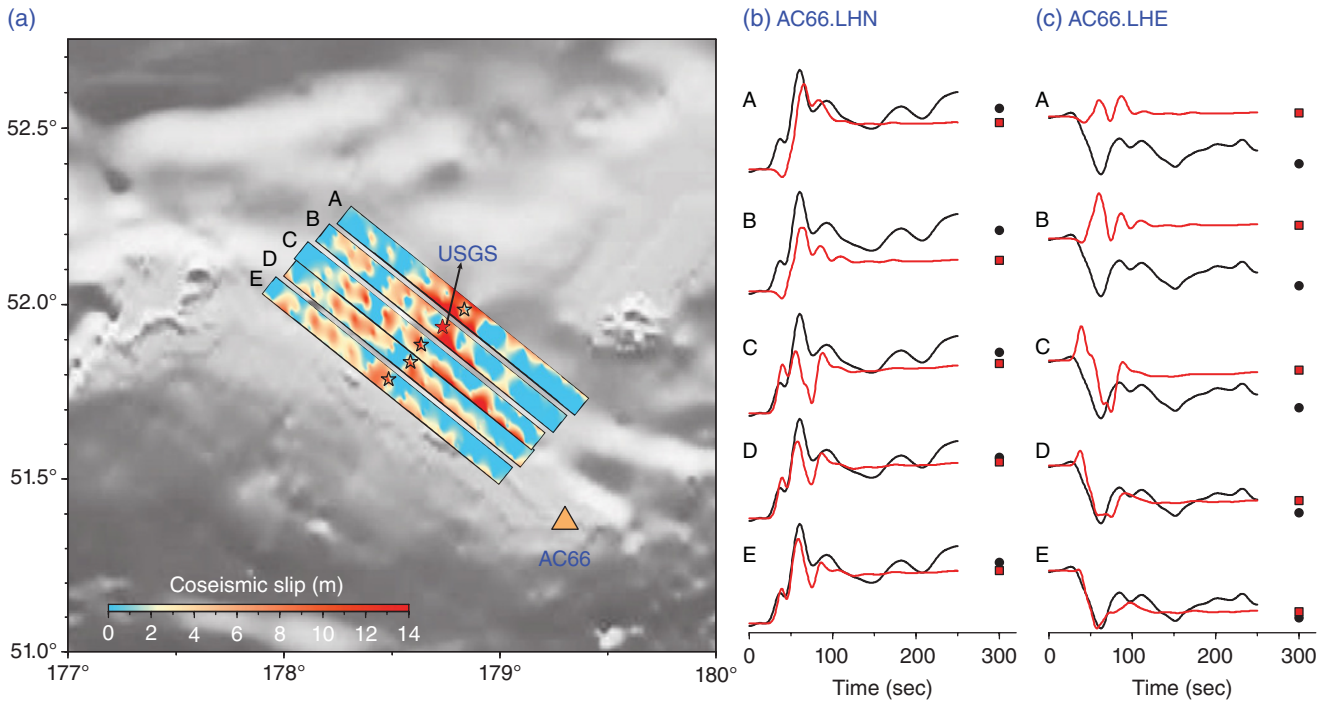
Figure 7.4 (a) Map view of five inverted slip distributions, A–E, using the steeply dipping fault plane for the 2014 Rat Islands earthquake with shifted hypocentral locations (stars), for joint inversions of teleseismic body waves, hr-GPS observations, and static displacement offsets (e.g., Fig. 7.7). The filled star shows the epicenter location from the USGS/NEIC catalog. Model E is the slip model on the steep fault plane shown in Figure 7.8. The position of local hr-GPS station AC66 is indicated by the triangle. (b) and (c) Comparisons of the observed north-south (LHN) and east-west (LHE) hr-GPS observations at station AC66 (black traces) and predicted waveforms (gray traces) for slip models A–E. The black dots and squares indicate the corresponding observed (daily averaged) and predicted static displacement offsets.

plane if we use a hypocenter depth of 95 km, compared to the USGS/NEIC hypocentral depth of 109 km, while we have similar fits for the steeply dipping fault using hypocenters at either 95 km or 109 km. The finite-fault inversion centroid depths vary with assumed hypocentral depth for both fault planes (Fig. 7.5c), and we find better agreement with the long-period seismic wave centroid estimates if we adopt 95 km and 109 km hypocentral depths for the shallowly and steeply dipping faults, respectively.

The finite-fault model from joint inversion using the shallowly dipping plane with a hypocentral depth of 95 km and the 25 km offset location is shown in Figure 7.6, with observed and predicted seismic and GPS signals shown in Figure 7.7. The finite-fault model from joint inversion using the steeply dipping plane with a hypocentral depth of 109 km and the 25 km offset location is shown in Figure 7.8, with corresponding signal comparisons in Figure 7.9. The moment rate functions are similar for both solutions, with a relatively low amplitude interval for ~15 s followed by a large triangular pulse with about 25 s duration. The slip distribution on the shallowly

dipping plane (Fig. 7.6) has about 9 m slip near the hypocenter and a 30 km × 20 km patch of large slip centered about 25 km downdip (toward the northwest), with peak slip of ~11 m. The gap in slip between the hypocenter and the main slip patch is consistently found for inversions with the shallowly dipping plane. The subfault source time functions within the region of significant slip activate at the rupture expansion velocity time, so it is an actual rupture velocity. The waveform matches in Figure 7.7 are quite good for P and SH waves apart from some of the early low amplitude P arrivals and the nodal P waveforms at azimuths to the southeast and northwest (along the slab strike). The EW motions at GPS sites AB01 and AB21 are fit adequately and good fits are found for the horizontal motions at AC60 and AC66, along with the vertical static offset at AC66. As indicated by Figure 7.5a, comparable waveform matches are found for hypocentral locations at or around the USGS/NEIC location, so this solution is quite stable and similar to that in *Ye et al.* [2014].

The slip distribution found for the steeply dipping plane (Fig. 7.8) also has some large slip near the
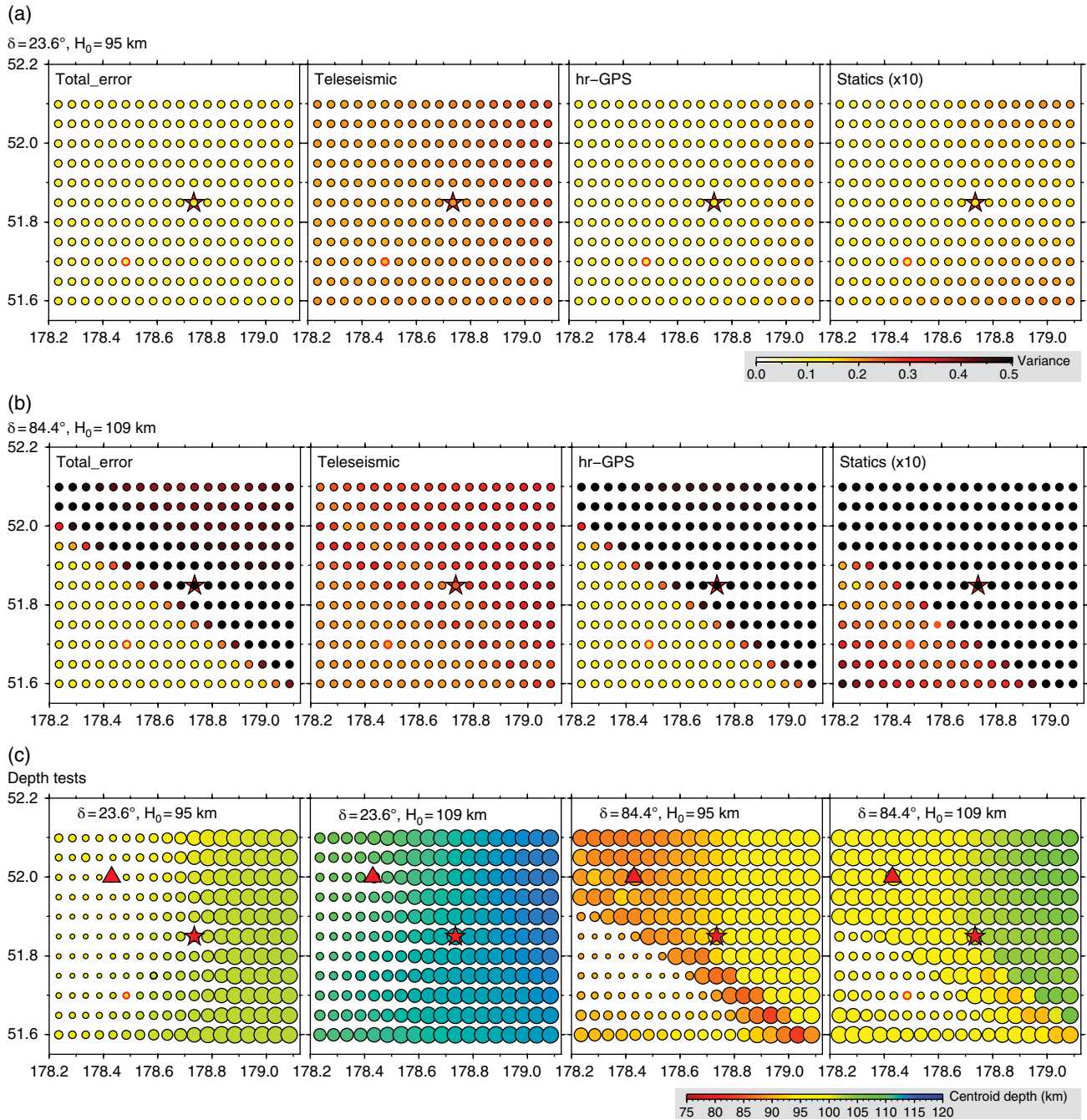
Figure 7.5 Spatial plots of residual waveform misfit of teleseismic body wave, hr-GPS, static offset, and all three datasets together (total) for inverted slip models using different assumed hypocentral locations (each point) on (a) the shallowly dipping fault plane with hypocentral depth 95 km and (b) the steeply dipping fault plane with hypocentral depth 109 km. (c) The centroid depth for the finite fault models for the shallowly dipping (dip, δ = 23.6°) and steeply dipping fault planes (δ = 84.4°) with hypocentral depths of 95 km or 109 km at different initial locations. The radius of the circles is scaled with the total residual waveform misfit, saturated with variance of 0.12. The black stars and triangles show the epicentral location from the USGS/NEIC catalog and the centroid location from gCMT catalog, respectively. The circles at around (178.5W, 51.7N) highlight the selected models shown in Figures 7.6 and 7.8, with initial location ~25 km SW of the USGS/NEIC epicenter.
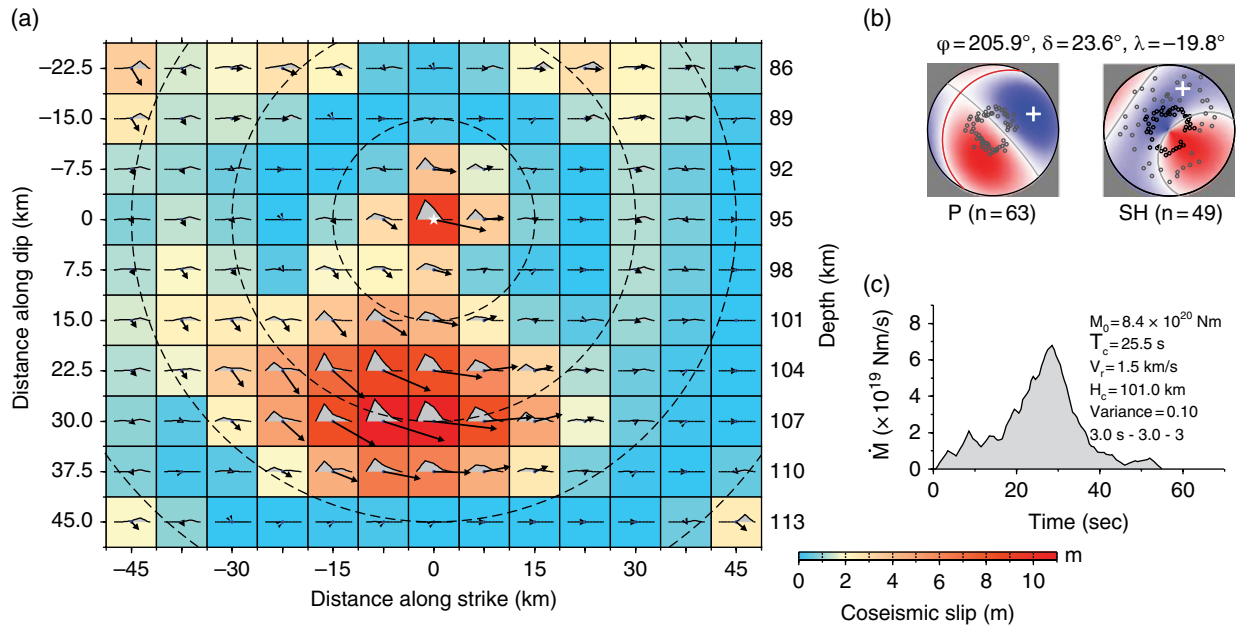
Figure 7.6 Finite-fault slip model for the shallowly dipping fault plane from the joint inversion of teleseismic body waves (P and SH), hr-GPS, and static displacement offsets for the 2014 M_w 7.9 Rat Islands earthquake. The slip distribution on the fault plane is shown with the arrows indicating average rake of each subfault, and slip magnitude being color coded. A rupture expansion velocity of V_r = 1.5 km/s is used, and the isochrones for the expanding rupture front in 10 s increments are indicated by the dashed circles. The moment-rate function, seismic moment, centroid time shift (T_c), and the average focal mechanism for each fault segment are shown, with lower hemisphere equal area projections indicating the positions sampled by teleseismic P and SH waves used in the inversions. Observed and synthetic waveform comparisons are shown in Figure 7.7. (*For color detail, please see color plate section*).

hypocenter, with peak slip of ~14 m, and a patch with peak slip of ~10 m at similar depth located to the northwest along strike. But this fault plane choice results in a widely spread slip distribution with a peak slip of ~11 m near 70 km depth, which is near the upper edge of the underthrust plate. The model domain is intentionally restricted so that it does not extend to depths above the subducted slab, but if we do allow shallower slip, the inversion tends to place some slip at the upper edge of the model. It is uncomfortable to have large slip at the edge of finite-fault models, but it is plausible that this broadening of slip is located within the subducted oceanic crust, which may have pore fluids that facilitate expansion of the rupture. The overall waveform matches for the steeply dipping fault (Fig. 7.9) are comparable to those for the shallowly dipping plane and the joint inversion residuals are very similar. The steeply dipping plane fits the nodal P wave data to the southeast a bit better than the shallowly dipping plane but has more severe waveform mismatches to the northwest, so it is very difficult to favor one geometry over another based on data mismatch.

The finite-fault seismic moment estimate is a bit lower for the shallowly dipping plane (8.4×10^{20} Nm) than for the steeply dipping plane (9.8×10^{21} Nm), but the centroid

time shifts of ~25.5–25.0 s, and average slip depths, H_c, ~101–96.8 km for the shallowly and steeply dipping planes, respectively, are compatible with values from the long-period point-source solutions. Given the simple earth structure, kinematic constraints, and simplified faulting representations used, the overall characteristics of all data are quite well modeled by either the shallowly or steeply dipping fault models. Map views of the two fault models, along with comparison of the observed and predicted GPS static motions are shown in Figure 7.10. The primary slip regions are located in the vicinity of the aftershock distribution, but the NE-SW spread of the aftershock distribution may somewhat favor the shallowly dipping fault geometry. These models are generally similar to those obtained from inversion of only teleseismic signals by *Ye et al.* [2014], but some of the isochronal smearing of slip apparent in the latter models is suppressed by the addition of the hr-GPS data and there are minor differences in seismic moment. The overall waveform matches are comparable.

Using the slip models from the two finite-fault inversions, we estimated the stress drop weighted by the slip distribution. *Noda et al.* [2013] show that the stress drop averaged this way is more appropriate for estimating the strain energy. We first computed the stress drop by
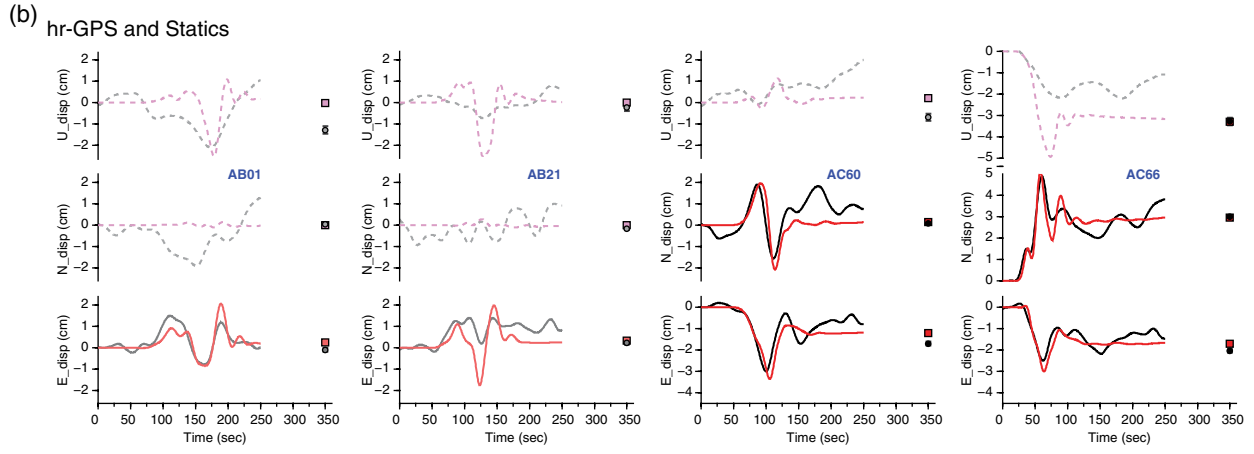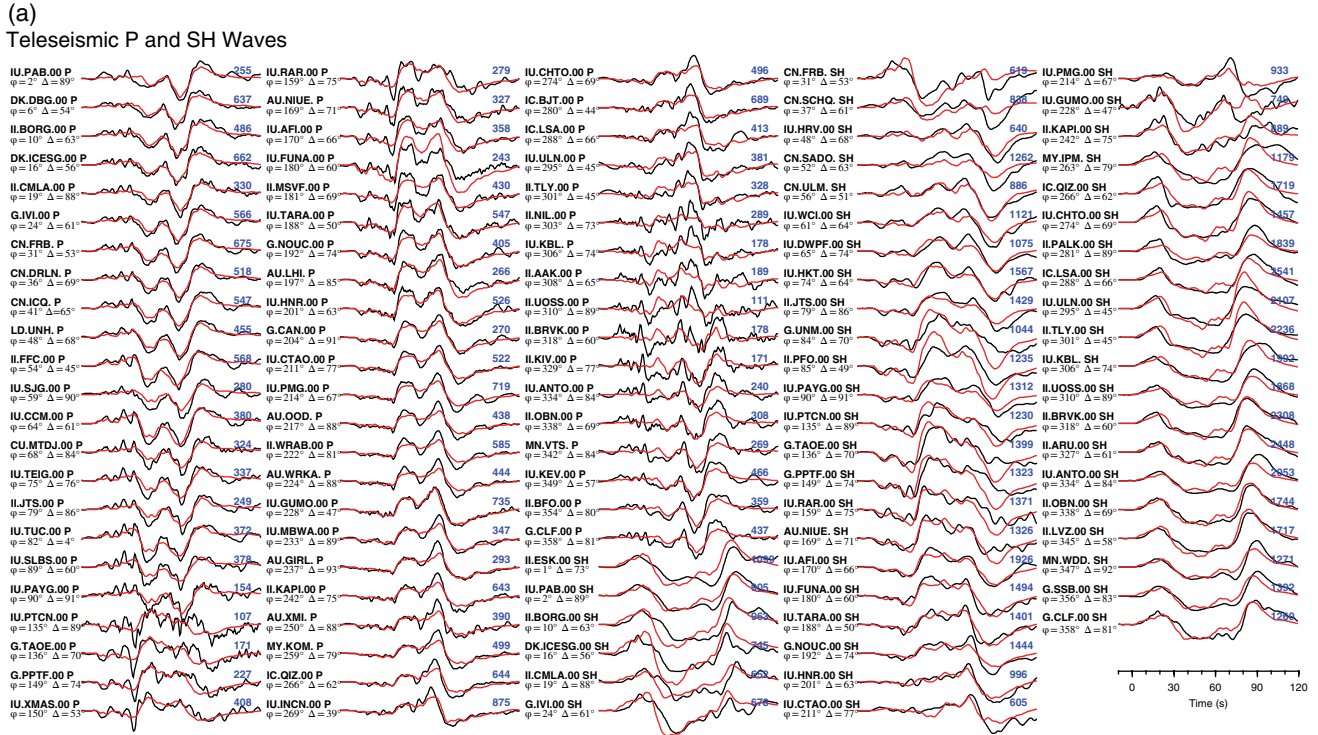
(a)
Teleseismic P and SH Waves

(b) hr-GPS and Statics

Figure 7.7 Comparison of (a) observed (black) and synthetic (gray) P and SH ground motions and (b) 1-Hz high-rate GPS ground motions and static displacement offsets for the selected rupture model on the shallowly dipping fault plane shown in Figure 7.6. For each station in (a), the azimuth from the source (φ) and epicentral distance (Δ) are indicated, along with the peak-to-peak ground motion in microns (numbers on the right). The observed signal amplitudes are normalized. The gray curves are true relative amplitude synthetic waveforms. For GPS observations in (b), both hr-GPS and static offsets of the NS and EW components at sites AC60 and AC66, and the vertical static offset at site AC66 have been given full weight in the joint inversion; and the EW component (hr-GPS and static offset) at more distant GPS sites, AB01 and AB21, have been given a low weight (about one third), in the inversion. The dashed curves show the other observed and forward modeled GPS observations, which are not used in the inversion, due to the low signal-to-noise ratio.

embedding our slip models in a homogeneous half space with an appropriate depth and geometry, and numerically computed the stress drop for the spatially heterogeneous slip distribution. The computation is based on the methods developed by *Mansinha and Smylie* [1971] and

Okada [1992]. The average stress drop estimates, are ~16.4 MPa and ~24.8 MPa for the slip models on the shallowly and steeply dipping faults, respectively. These values are consistent with stress drop estimates obtained from a slip model with trimming threshold ξ ~0.15 to 0.2,
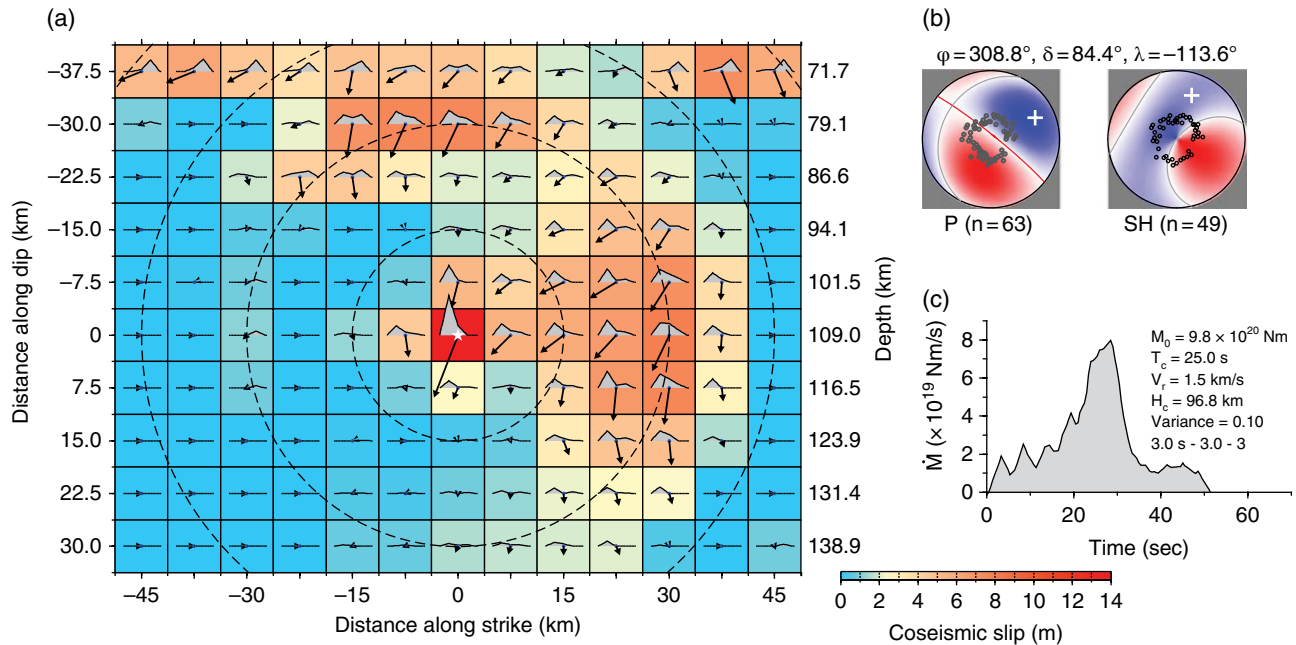
Figure 7.8 Finite-fault slip model for the steeply dipping fault plane from the joint inversion of teleseismic body waves (P and SH), hr-GPS, and static displacement offsets for the 2014 M_w 7.9 Rat Islands earthquake. Format is the same as in Figure 7.6. (*For color detail, please see color plate section*).

in which the stress drop is estimated for a circular crack model with the area given by summing the subfaults with a moment larger than ξ times the moment of the subfault with the largest moment. These stress drop estimates are very dependent on the rupture area, and that, in turn, is dependent on the rupture expansion velocity. We performed inversions with varying rupture velocity for both fault models, scaling the grid spacing proportional to the rupture velocity so that the slip distribution shapes are similar but the areas vary systematically. Estimates of the average stress drop from the heterogeneous slip models are shown in Figure 7.11a, with expected large variation. By computing radiated energy, we can explore radiation efficiency constraints on the rupture expansion velocity.

7.1.3. Seismic Radiated Energy

The average source spectrum and estimated total radiated energy are shown in Figure 7.12a. The source spectrum at frequencies less than ~0.05 Hz is obtained from the moment rate function from the finite-fault inversion (here we use the shallowly dipping fault plane solution from Fig. 7.6) and at frequencies of 0.05 – 2 Hz from the stack average of broadband P wave displacement spectra, corrected for the radiation pattern and an attenuation operator, t* = travel time/Q, where Q is the quality factor

defined by loss of amplitude per cycle. Large uncertainties are introduced by limited knowledge of the average P and S wave velocities around the source, as well as limited data bandwidth and uncertainty in propagation corrections, particularly for attenuation. Relatively low attenuation is expected for the 2014 Rat Islands earthquake because of the source depth and location within the steeply dipping subducting slab traversed by the down-going P signals. To estimate t*, we downward interpolate the t*(f) model of *Perez-Campos et al.* [2003] from a depth of 50 km to halved values at 650 km. This provides consistent values with the empirical Green's function corrected radiated energy for the great M_w 8.3 deep Sea of Okhotsk earthquake [*Ye et al.*, 2013b]. For the 2014 Rat Islands event, which is not very deep, the frequency-dependent t* model has t*~1.0 s, 0.9 s, and 0.5 s at frequencies of 0.01 Hz, 0.1 Hz, and 2 Hz, respectively.

The average source spectrum for this earthquake is slightly enriched in high-frequency spectral level relative to a reference ω–squared source spectrum with a stress parameter of 3 MPa. The measured total radiated seismic energy for frequencies less than 2 Hz is, E_R ~1.8 × 10^{16} J. This was estimated using the energy fraction computed for high-frequency teleseismic P wave ground velocity spectra relative to the low-frequency energy content following the theory and method of *Venkataraman and*
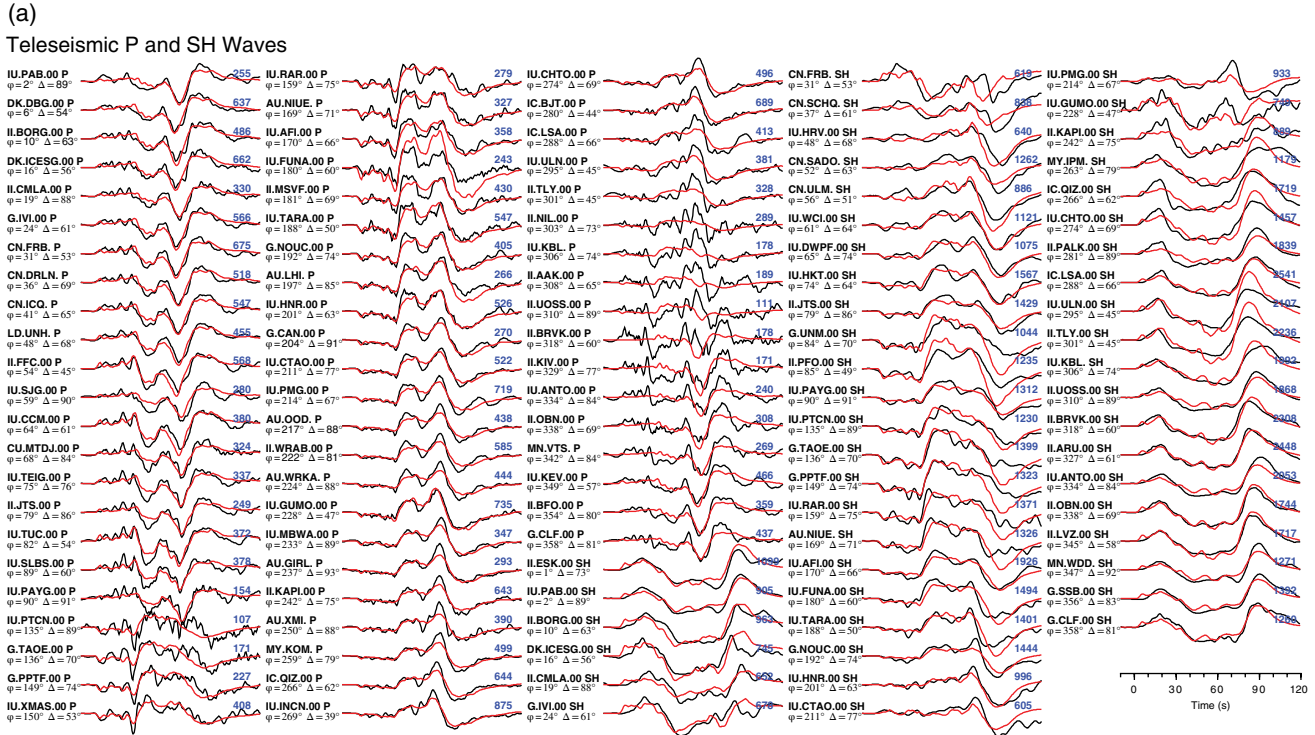
Figure 7.9 Comparisons of (a) observed (black) and synthetic (gray) P and SH ground motions and (b) 1-Hz high-rate GPS ground motions along with static displacement offsets for the selected rupture model on the steeply dipping fault plane shown in Figure 7.8. Format is the same as in Figure 7.7.

Kanamori [2004]. This estimate falls within the range of 1.1×10^{16} J– 2.7×10^{16} J found assuming constant t* values of 0.7 s to 0.4 s [*Ye et al.*, 2014]. The corresponding seismic moment-scaled radiated energy ratio is $E_R/M_0 = 1.85 \times 10^{-5}$. This is near the low end of typical values for large intraplate earthquakes (average $\sim 3.0 \times 10^{-5}$), and near the upper end of typical large interplate event values (average $\sim 1.5 \times 10^{-5}$) [e.g., *Ye et al.*, 2012].

7.2. DISCUSSION AND CONCLUSIONS

Joint inversions of teleseismic body waves, regional hr-GPS (1Hz) recordings, and their corresponding static displacement offsets for the 2014 Rat Islands earthquake, yield slip distributions with a compact slip zone spanning 50 km × 30 km with a maximum slip of ~11 m for a shallowly dipping plane, or a more distributed slip pattern
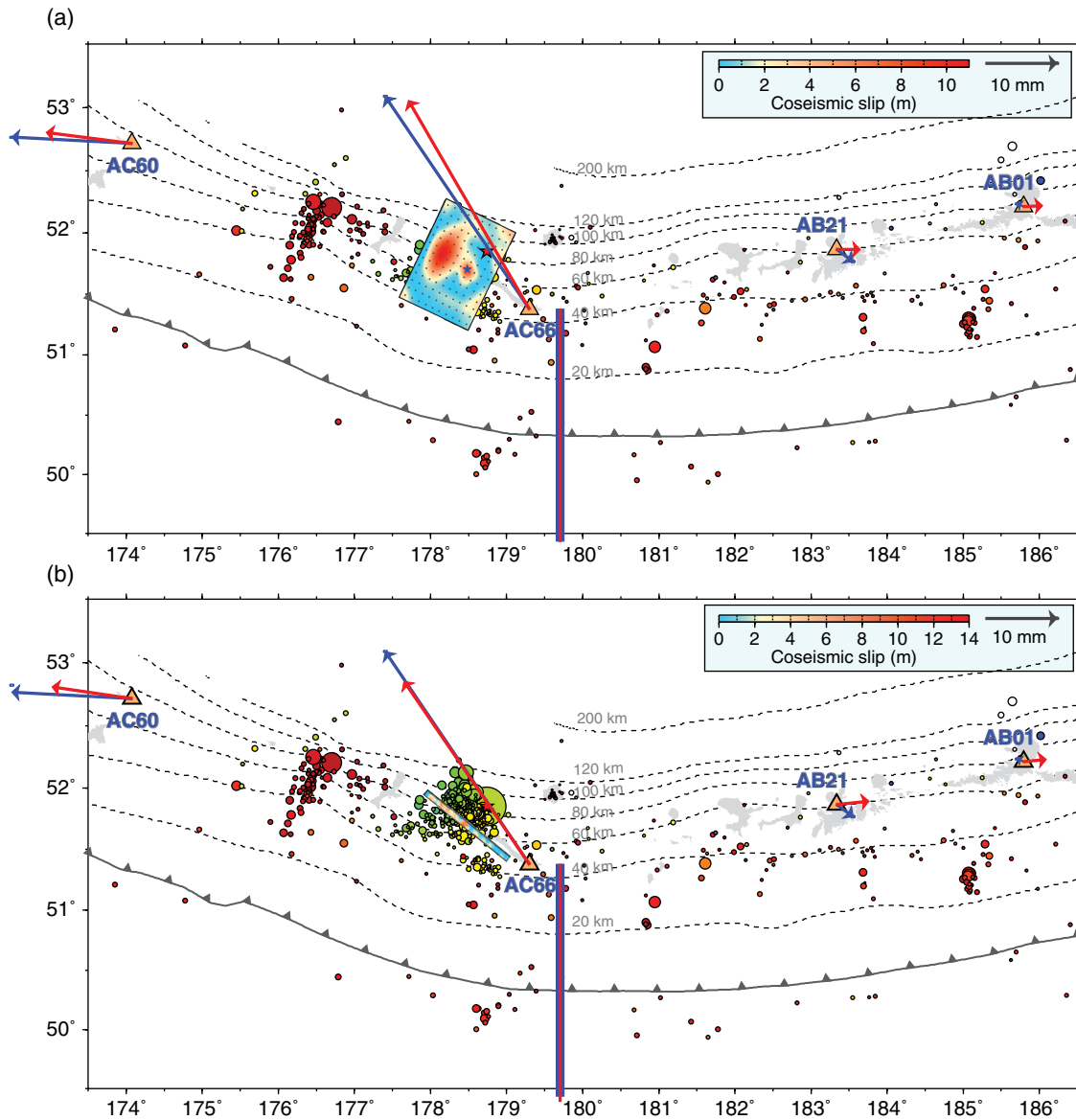
Figure 7.10 Map of the selected (a) shallowly dipping and (b) steeply dipping fault slip models for the 2014 M_w 7.9 Rat Islands earthquake from Figures 7.6 and 7.8, respectively, along with the aftershock sequence from Figure 7.2. The observed and predicted horizontal static ground motions at the 4 hr-GPS sites used in the joint inversion are shown with arrows. The bars show the observed (thicker bar) and predicted (narrower bar) vertical displacement offset at site AC66. The stars show the epicenter from the USGS/NEIC catalog and the epicenter of the finite fault models, respectively.

extending upward to ~70 km, with maximum slip of ~14 m on a steeply dipping plane. Maximum slip is not a well-resolved parameter in finite fault inversions, as it depends on model parameterization. The values given here are for the 7.5 km × 7.5 km grid spacing of our models. The centroid depths, centroid time shifts, and total seismic moment from both slip models are comparable with values determined from long-period seismic waves.

Radiation efficiency, proportional to the ratio between the moment-scaled radiated energy and static stress drop, has been used in evaluating heating effects, which are important for considering possible physical mechanisms for intermediate-depth and deep earthquakes in very high pressure and temperature environments [e.g., *Kanamori et al.*, 1998; *Ye et al.*, 2013b]. However, as apparent in Figure 7.11a, there is large uncertainty in estimating
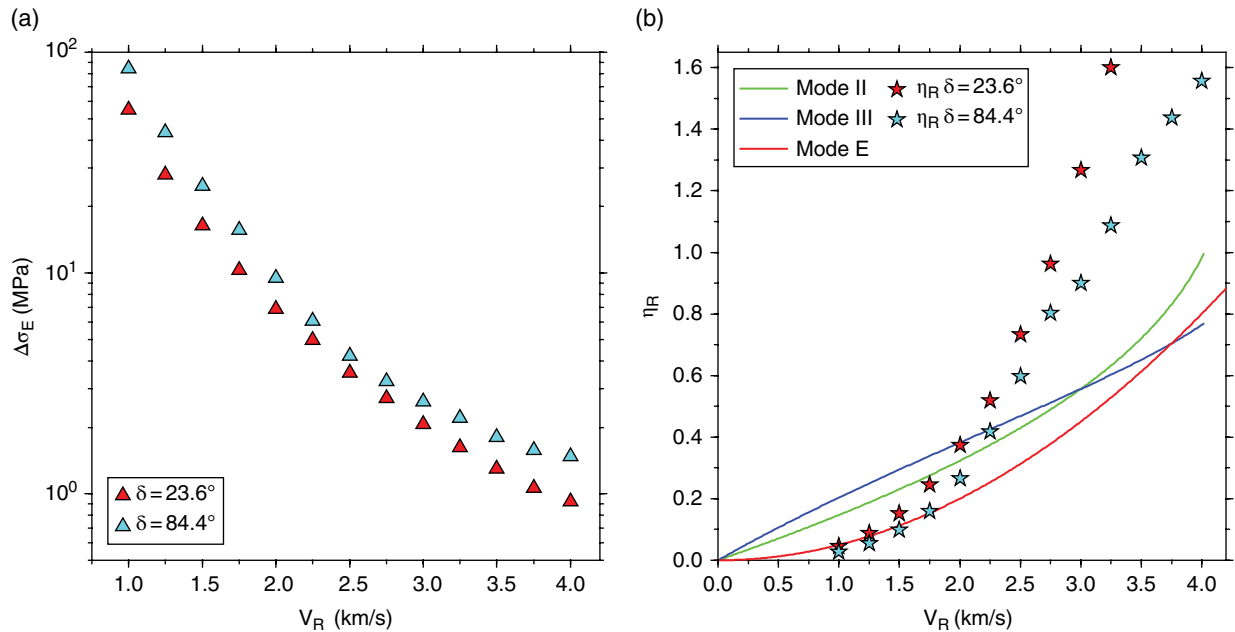
Figure 7.11 Variation of (a) calculated average stress drop and (b) radiation efficiency as functions of assumed rupture expansion velocity for finite-fault models using the shallowly dipping and steeply dipping fault planes. The curves in (b) show the predicted radiation efficiency with reference shear-wave velocity ~4.5 km/s for mode II and III cracks, and an energy-based model (mode E). The radiated seismic energy, 1.8×10^{18} J, estimated from the spectrum method (Fig. 7.12a), and seismic moment from gCMT catalog are used to estimate the radiation efficiencies. For our selected models with V_R 1.5 km/s shown in Figures 7.6 and 7.8, the stress drops are ~16.4 MPa and ~24.8 MPa, and the radiation efficiencies are ~0.15 and ~0.10, for the shallowly and steeply dipping fault planes, respectively.

static stress drops from finite-fault slip distributions for this event, mainly due to lack of directivity effects and resulting poor constraint on the rupture areas.

There are strong trade-offs between the rupture velocity and subfault source time function parameters, and subfault grid size in our finite-fault parameterization method. Estimated stress drop decreases dramatically with increasing rupture expansion velocity for finite-fault slip models on the shallowly and steeply dipping planes that give comparable fits of the observations. Comparison of the corresponding radiation efficiency for Mode II and III cracks suggests that a rupture velocity around 1.5 to 2.0 km/s is favored (Fig. 7.11b). This supplements the finding that slip models for a 1.5 km/s rupture expansion rate have large-slip areas compatible with the spatial extent of the aftershock distribution (Fig. 7.10). We infer that a rupture velocity, Vr = 1.5 km/s, as used in our selected models, is reasonable.

The corresponding radiation efficiency estimates are ~0.15 and ~0.10 for the static stress drops of ~16.4 MPa and ~24.8 MPa for the slip models on the shallowly and steeply dipping fault planes, respectively. The low radiation efficiency and high stress drop suggest that a relatively dissipative source process, possibly involving

melting or thermal shear runaway [e.g., *Prieto et al.*, 2013], occurred during the 2014 Rat Islands event.

Reactivation of inherited oceanic faults formed at shallow depths has been commonly invoked to account for intermediate-depth faulting. Shallow intraplate faulting, such as the large M_w 7.6 trench slope normal faulting earthquake on 30 March 1965 (Fig. 7.2a), may provide hydrated fault zones that can be reactivated as the slab sinks to intermediate depths and undergoes dehydration reactions that release fluids, reducing confining stresses on the fault zone [*Peacock*, 2001]. Observations supporting this scenario involve similarity of the fault orientations relative to the plate surface [e.g., *Warren*, 2014]. However, the faulting orientations for the 2014 Rat Islands event are not easily related to the likely geometry of shallow plate bending faults, with the deeper slab either displacing northeastward on the shallow-dipping plane or almost vertically downward on the steeply dipping plane, at relatively low angle to the slab surface. Given the obliquity of the relative plate motions along the curving Aleutian trench, contortion of the subducted Pacific plate [e.g., *Creager and Boyd*, 1991; *Ruppert et al.*, 2012] is expected to affect the intraplate stresses in the slab beneath the Rat Islands archipelago, but the faulting
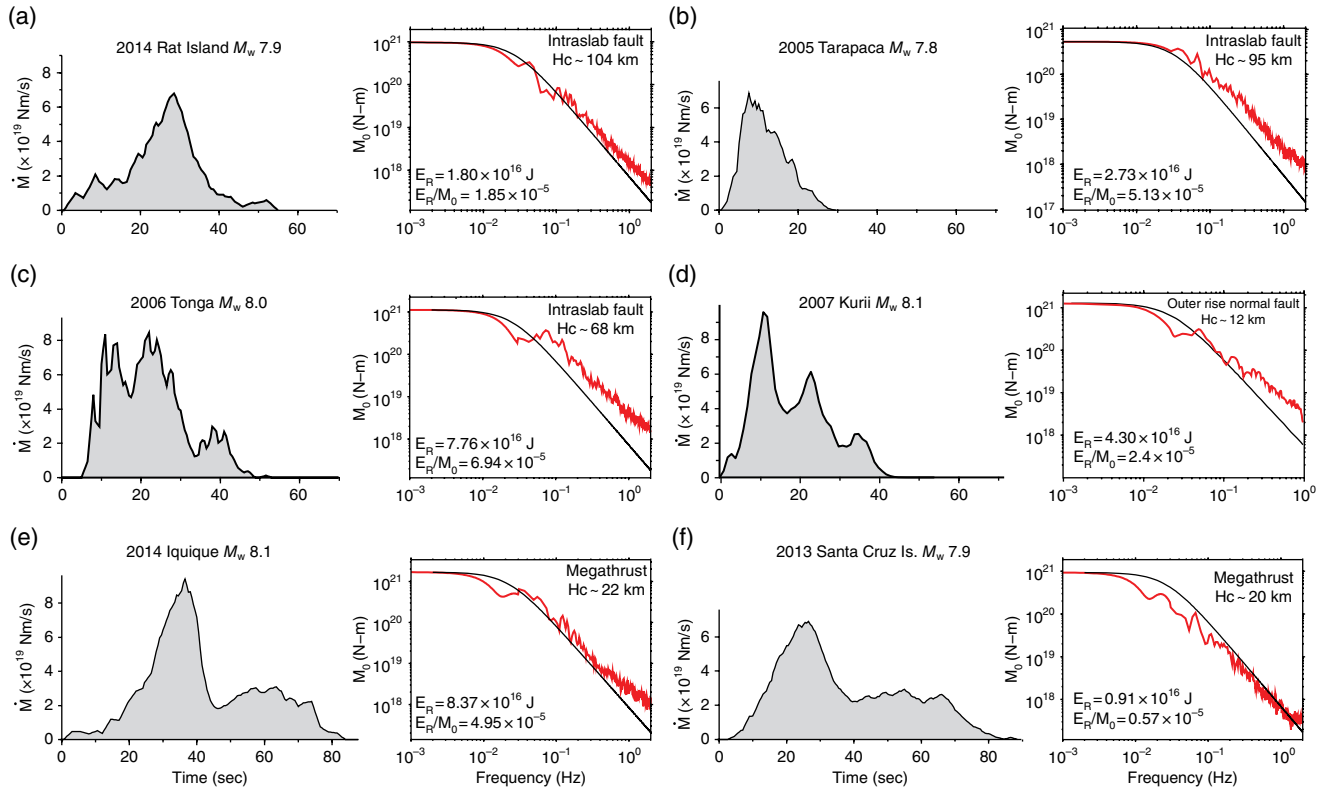
Figure 7.12 Comparison of moment rate functions and source spectra for (a) the 23 June 2014 Rat Islands intraslab earthquake (M_w 7.9), (b) the 13 June 2005 Tarapaca intraslab earthquake (M_w 7.8), (c) the 3 May 2006 Tonga intraslab earthquake (M_w 8.0), (d) the 13 January 2007 Kuril outer rise intraplate earthquake (M_w 8.1) [*Ammon et al.*, 2008], (e) the 1 April 2014 Iquique interplate earthquake (M_w 8.1), and (f) the 6 February 2013 Santa Cruz Island interplate earthquake [M_w 7.9; *Lay et al.*, 2013]. The centroid depth (H_c) for each earthquake is from gCMT catalog. Reference ω-squared spectra for a 3 MPa stress parameter and seismic moment of each event are shown by the smooth black curves.

may be controlled by inherited fault zone structure. Even if correct in general, reactivation of prior fault systems does not provide a simple strain accumulation and release context like that for the relative plate motions driving megathrust faulting to provide guidance on the frequency of large intermediate depth events. The best approach seems to characterize the attributes of such events based on the limited number of recorded examples and to recognize their general potential in circum-Pacific earthquake hazard assessments.

Figure 7.12 shows comparisons of source time functions from finite-fault inversions and teleseismic source spectra for the 2014 Rat Islands earthquake and similar magnitude events in different tectonic regions, such as the 13 June 2005 Tarapaca, Chile intraslab earthquake (M_w 7.8), the 3 May 2006 Tonga intraslab earthquake (M_w 8.0), the 13 January 2007 Kuril outer rise intraplate earthquake (M_w 8.1) [*Ammon et al.*, 2008], the 1 April 2014 Iquique interplate earthquake (M_w 8.1), and the 6 February 2013 Santa Cruz Islands interplate earthquake (M_w 7.9) [*Lay et al.*, 2013]. Compared to a typical

megathrust earthquake like the 2013 Santa Cruz earthquake and to reference 3 MPa ω-squared spectra, the intraslab earthquakes are generally enriched in high-frequency seismic radiation, which contributes to strong ground shaking damage. Both high stress drop and low attenuation along some wave paths under the arc may contribute to strong shaking [*Ye et al.*, 2013a]. The 2014 Iquique event has an unusually spatially-concentrated slip distribution for a megathrust event, and it also has a somewhat enriched high-frequency source spectrum, so the Rat Islands spectrum is not particularly distinctive, as indicated by the E_R/M_0 value.

Comparisons of teleseismic P waveforms from several large intermediate depth earthquakes demonstrate the overall similarity of the 2014 Rat Islands event signals to events in other regions [*Ye et al.*, 2014]. *Ye et al.* [2014] show the widespread distribution of large intermediate-depth earthquakes at depths from 70 km to 200 km with $M_w \geq 7.5$ dating back to 1900, demonstrating the global extent of this class of earthquakes and the proximity to population centers.

Each region likely has unique tectonic stresses and inherited faulting geometries from shallower plate bending, making it difficult to infer recurrence times or total distribution of such events from the short seismological record. However, recognition of this class of infrequent large ruptures should be incorporated into seismic hazard assessments in populated subduction zone environments.

ACKNOWLEDGEMENTS

REFERENCES

Abe, K. (1972), Lithospheric normal faulting beneath the Aleutian trench, *Phys. Earth Planet. Inter.*, *5*, 190–198.

Allen, T. I., K. D. Marano, P. S. Earle, and D. J. Wald (2009), PAGER-CAT: A composite earthquake catalog for calibrating global fatality models, *Seism. Res. Lett.*, *80*, 57–62, doi:10.1785/gssrl.80.1.57.

Ammon, C. J., H. Kanamori, and T. Lay (2008), A great earthquake doublet and seismic stress transfer cycle in the central Kuril islands, *Nature*, *451*(7178), 561–565.

Bassin, C., G. Laske, and G. Masters (2000), The Current Limits of Resolution for Surface Wave Tomography in North America, *EOS Trans AGU*, *81*, F897.

Beck, S. L., and D. H. Christensen (1991), Rupture process of the February 4, 1965, Rat Islands earthquake, *J. Geophys. Res.*, *96*, 2205–2221.

Carver, G., and G. Plafker (2008), *Paleoseismicity and Neotectonics of the Aleutian Subduction Zone—An Overview, in Active Tectonics and Seismic Potential of Alaska* (eds J. T. Freymueller, P. J. Haeussler, R. L. Wesson and G. Ekström), American Geophysical Union, Washington, D. C. doi:10.1029/179GM03.

Craig, T. J., A. Copley, and J. Jackson (2014), A reassessment of outer-rise seismicity and its implications for the mechanics of oceanic lithosphere, *Geophys. J. Int.*, *197*, 63–89, doi:10.1093/gji/ggu013.

Creager, K. C., and T. M. Boyd (1991), The geometry of Aleutian subduction: Three-dimensional kinematic flow model, *J. Geophys. Res.*, *96*, 2293–2307.

Cross, R. S., and J. T. Freymueller (2008), Evidence for and implications of a Bering plate based on geodetic measurements from the Aleutians and western Alaska, *J. Geophys. Res.*, *113*(B7).

Delouis, B., and D. Legrand (2007), M_w 7.8 Tarapaca intermediate depth earthquake of 13 June 2005 (northern Chile): Fault plane identification and slip distribution by waveform inversion, *Geophys. Res. Lett.*, *34*, L01304, doi:10.1029/2006GL028193.

DeMets, C., R. G. Gordon, and D. F. Argus (2010), Geologically current plate motions. *Geophys. J. Int.*, *181*: 1–80. doi:10.1111/j.1365–246X.2009.04491.x.

Ding, K., J. T. Freymueller, Q. Wang, and R. Zou (2015), Coseismic and early postseismic deformation of the 5 January 2013 Craig Mw 7.5 earthquake from static and kinematic GPS solutions, *Bull. Seismol. Soc. Am*, *105*(2B), 1153–1164.

Dziewonski, A. M., and D. L. Anderson (1981), Preliminary reference Earth model, *Phys. Earth Planet. Inter.*, *25*(4), 297–356.

Ekström, G., and E. R. Engdahl (1989), Earthquake source parameters and stress distribution in the Adak Island region of the central Aleutian Islands, Alaska, *J. Geophys. Res.*, *94*(B11), 15499–15519, doi:10.1029/JB094iB11p15499.

Engdahl, E. R., R. van der Hilst, and R. Buland (1998), Global teleseismic earthquake relocation with improved travel times and procedures for depth determination, *Bull. Seismol. Soc. Am.*, *88*(3), 722–743.

Fu, Y., and J. T. Freymueller (2012), Seasonal and Long-term Vertical Deformation in the Nepal Himalaya Constrained by GPS and GRACE Measurements, *J. Geophys. Res.*, *117*, B03407, doi:10.1029/2011JB008925.

Gabsatarov, Y. V., G. M. Steblov, and D. I. Frovlov (2011), The new GPS evidence for the region of Bering Microplate, *Phys. Solid Earth*, *49*, 114–118.

Geist, E. L., J. R. Childs, and D. W. Scholl (1988), The origin of summit basins of the Aleutian Ridge: Implications for block rotation of an arc massif, *Tectonics*, *7*(2), 327–341.

Hartzell, S. H., and T. H. Heaton (1983), Inversion of strong ground motion and teleseismic waveform data for the fault rupture history of the 1979 Imperial Valley, California, earthquake, *Bull. Seismol. Soc. Am.*, *73*(6A), 1553–1583.

Hayes, G. P., D. J. Wald, and R. L. Johnson (2012), Slab1.0: A three-dimensional model of global subduction zone geometries, *J. Geophys. Res.*, *117*, B01302, doi:10.1029/2011JB008524.

Herrmann, R. B. (2013), Computer programs in seismology: An evolving tool for instruction and research, *Seism. Res. Lett.*, *84*, 1081–1088, doi:10.1785/0220110096.

Johnson, J. M., Y. Tanioka, L. J. Ruff, K. Satake, H. Kanamori, and L. R. Sykes (1994), The 1957 great Aleutian earthquake, *Pure Appl, Geophys.*, *142*, 3–28.

Kanamori, H. (1971), Seismological evidence for a lithospheric normal faulting – the Sanriku earthquake of 1933, *Phys. Earth Planet. Inter.*, *4*(289), 300.

Kanamori, H., and L. Rivera (2008), Source inversion of W phase: speeding up seismic tsunami warning, *Geophys. J. Inter.*, *175*, 222–238.

Kanamori, H., D. L. Anderson, and T. H. Heaton (1998), Frictional melting during the rupture of the 1994 Bolivian earthquake, *Science*, *279*(5352), 839–842.

Kanamori, H., W. H. K. Lee, and K.-F. Ma (2012), The 1909 Taipei earthquake – implications for seismic hazard in Taipei, *Geophys. J. Int.*, *191*, 126–146, doi:10.1111/j.1365-246X.2012.05589.x.

Kausel, E., and J. Campos (1992), The *Mw* = 8 tensional earthquake of 9 December 1950 of northern Chile and its relation to the seismic potential of the region, *Phys, Earth and Planetary Interiors*, *72*, 220–235.

Kikuchi, M., and H. Kanamori (1991), Inversion of complex body waves—III, *Bull. Seismol. Soc. Am.*, *81*(6), 2335–2350.

Kuge, K., and H. Kawakatsu (1992), Deep and intermediate-depth non-double couple earthquakes: interpretation of

moment tensor inversions using various passbands of very broadband seismic data, *Geophys. J. Inter.*, *111*(3), 589–606.

Lay, T., C. J. Ammon, H. Kanamori, M. J. Kim, and L. Xue (2011), Outer trench-slope faulting and the 2011 *Mw* 9.0 off the Pacific coast of Tohoku Earthquake, *Earth Planets Space*, *63*, 713–718, doi:10.5047/eps.2011.05.006.

Lay, T., H. Kanamori, C. J. Ammon, A. R. Hutko, K. Furlong, and L. Rivera (2009), The 2006–2007 Kuril Islands great earthquake sequence, *J. Geophys. Res.*, *114*, B113208, doi:10.1029/2008JB006280.

Lay, T., L. Astiz, H. Kanamori, and D. H. Christensen (1989), Temporal variation of large intraplate earthquakes in coupled subduction zones, *Phys. Earth Planet. Inter.*, *54*, 258–312.

Lay, T., L. Ye, H. Kanamori, Y. Yamazaki, K. F. Cheung, and C. Ammon (2013), The February 6, 2013 *Mw* 8.0 Santa Cruz Islands earthquake and tsunami, *Tectonophysics*, *608*, 1109–1121.

Mackey, K. G., K. Fujita, L. V. Gunbina, V. N. Kovalev, V. S. Imaev, B. M. Koz'min, and L. P. Imaeva (1997), Seismicity of the Bering Strait Region: evidence for a Bering Block, *Geolog. Soc. Amer. Bull.*, *25(11)*, 979–982, doi:10.1130/0091-7613(1997)025.

Mansinha, L., and D. E. Smylie (1971), The displacement fields of inclined faults, *Bull. Seismol. Soc. Am.*, *61*(5), 1433–1440.

McCloskey, J., D. Lange, F. Tilmann, S. S. Nalbant, A. F. Bell, D. H. Natawidjaja, and A. Rietbrok (2010), The September 2009 Padang earthquake, *Nature Geoscience*, *3*, 70–71, doi:10.1038/ngeo753.

Noda, H., N. Lapusta, and H. Kanamori (2013), Comparison of average stress drop measures for ruptures with heterogeneous stress change and implications for earthquake physics, *Geophys. J. Int.*, *193*, 1691–1712, doi:10.1093/gji/ggt074.

Okada, Y. (1992), Internal deformation due to shear and tensile faults in a half-space, *Bull. Seism. Soc. Am.*, *82*, 1018–1040.

Okal, E. A. (2005), A re-evaluation of the great Aleutian and Chilean earthquakes of 1906 August 17, *Geophys. J. Int.*, *161*(2), 268–282.

Papadopoulos, G. A., and A. Vassilopoulou (2001), Historical and archeological evidence of earthquakes and tsunamis felt in the Kythira strait, Greece, in *Tsunami Research at the End of a Critical Decade*, pp. 119–113, Springer.

Peacock, S. M. (2001), Are the lower planes of double seismic zones caused by serpentine dehydration in subducting oceanic mantle? *Geology*, *29*(4), 299–302.

Prieto, G. A., M. Florez, S. A. Barrett, G. C. Beroza, P. Pedraza, J. F. Blanco, and E. Poveda (2013), Seismic evidence for thermal runaway during intermediate-depth earthquake rupture, *Geophys. Res. Lett.*, *40*, 6064–6068, doi:10.1002/2013GL058109.

Redfield, T. F., D. W. Scholl, P. G. Fitzgerald, and M. E. Beck Jr. (2007), Escape tectonics and the extrusion of Alaska: Past, present and future, *Geology*, *35*(11), 1039–1042, doi:10.1130/G23799A.1.

Ruppert, N. A., N. P. Kozyreva, and R. A. Hansen (2012), Review of crustal seismicity in the Aleutian Arc and implications for arc deformation, *Tectonophysics*, *522*, 150–157.

Sleep, N. H. (2012), Constraint on the recurrence of great outer-rise earthquakes from seafloor bathymetry, *Earth Planets Space*, *64*, 1245–1246.

Storchak, D. A., D. Di Giacomo, I. Bondár, E. R. Engdahl, J. Harris, W. H. K. Lee, A. Villaseñor, and P. Bormann (2013), Public Release of the ISC-GEM Global Instrumental Earthquake Catalogue (1900–2009), *Seism. Res. Lett.*, *84*(5), 810–815, doi: 10.1785/0220130034.

Sykes, L. R. (1971), Aftershock zones of great earthquakes, seismicity gaps, and earthquake prediction for Alaska and the Aleutians, *J. Geophys. Res.*, *76*(32), 8021–8041.

Venkataraman, A., and H. Kanamori (2004), Observational constraints on the fracture energy of subduction zone earthquakes, *J. Geophys. Res.*, *109*, B05302, doi:10.1029/2003JB002549.

Warren, L. M. (2014), Dominant fault plane orientations of intermediate-depth earthquakes beneath South America, *J. Geophys. Res.*, *119*(7), 5762–5785.

Welc, J. L., and T. Lay (1987), The source rupture process of the Great Banda Sea earthquake of November 4, 1963, *Phys. Earth Planet. Inter.*, *45*, 242–254.

Wu, F. T., and H. Kanamori (1973), Source mechanism of February 4, 1965, Rat Island earthquake, *J. Geophys. Res.*, *78*, 6082–6092.

Ye, L., T. Lay and H. Kanamori (2012), Intraplate and interplate faulting interactions during the August 31, 2012, Philippine Trench earthquake (M_w 7.6) sequence, *Geophys. Res. Lett.*, *39*, L24310, doi:10.1029/2012GL054164.

Ye, L., T. Lay, and H. Kanamori (2013a), Ground shaking and seismic source spectra for large earthquakes around the megathrust fault offshore of northeastern Honshu, Japan, *Bull. Seismol. Soc. Am.*, *103*, no. 2B, 1221–1241, doi: 10.1785/0120120115.

Ye, L., T. Lay, and H. Kanamori (2014), The 23 June 2014 *Mw* 7.9 Rat Islands archipelago, Alaska, intermediate depth earthquake, *Geophys. Res. Lett.*, *41*, 6389–6395, doi:10.1002/2014GL061153.

Ye, L., T. Lay, H. Kanamori, and K. D. Koper (2013b), Energy release of the 2013 *Mw* 8.3 Sea of Okhotsk earthquake and deep slab stress heterogeneity, *Science*, *341*, 1380–1384.

Zhang, J., and T. Lay (1989), Duration and depth of faulting of the 22 June 1977 Tonga earthquake, *Bull. Seism. Soc. Am.*, *79*, 41–66.

Zumberge, J. F., M. B. Heflin, D. C. Jefferson, M. M. Watkins, and F. H. Webb (1997), Precise point positioning for the efficient and robust analysis of GPS data from large networks, *J. Geophys. Res.*, *102*(B3), 5005–5017, doi:10.1029/96JB03860.